Coherent Dual-Band Microwave Pulse Signal Generation Based on an Actively Mode-Locked Optoelectronic Oscillator

Changlong Du, Shifeng Liu, Li Yang, Mingzhen Liu, Liangzun Tang, Hao Chen, and Shilong Pan, *Fellow, IEEE*

***Abstract*—We propose and experimentally demonstrate a novel method for coherent dual-band microwave pulse signal generation with variable repetition rates based on an actively mode-locked optoelectronic oscillator (OEO). In the proposed structure, the carrier frequencies of the dual-band signal are determined by a dual-band bandpass filter (DB-BPF) embedded in the OEO loop. Stable oscillation and phase coherence between the two carrier frequencies are achieved through mutual frequency conversion and energy coupling induced by an injection signal applied to the intracavity MachZehnder modulator (MZM), whose frequency equals the interval between the two carriers. Simultaneously, microwave pulse signal generation is realized by applying an additional low-frequency electrical waveform to the bias port of MZM for active mode-locking. This signal is tuned so that its frequency aligns with an integer multiple of the oscillation loop's free spectral range (FSR). In a proof-of-concept experiment, coherent dual-band microwave pulse signals with carrier frequencies of 10 and 16.091 GHz are generated. Different pulses repetition rates of 100.3, 200.6, and 501.5 kHz are achieved through fundamental, second-order harmonic, and fifth-order harmonic mode-locking, respectively. Furthermore, coherent dual-band staggered double-pulses within one cavity period are successfully generated. The phase noise of the generated microwave pulse signal was measured to be below −139 dBc/Hz at a 10 kHz offset frequency.**

***Index Terms*—Active mode-locking, coherent, dual-band, optoelectronic oscillator (OEO), staggered pulse.**

I. Introduction

COHERENT dual-band microwave pulsed signals are essential for next-generation radar systems, offering superior performance in target detection, classification, and tracking across diverse and demanding scenarios [1], [2], [3]. By leveraging multiple frequency bands, such signals enable multimodal detection, enhance spatial and temporal resolution, and significantly improve sensitivity for range and velocity measurements. In addition, the inherent frequency diversity strengthens antistealth capability against low-observable targets and enhances resilience against electronic countermeasures, delivering robust antijamming performance in complex electromagnetic environments [4], [5]. These advantages make coherent dual-band microwave pulsed signals a key enabling technology of advanced radar technologies [1].

Conventional electronic techniques for generating coherent dual-band microwave pulse signals include direct digital synthesis (DDS) [6], phase-locked loops (PLLs) [7], and voltage-controlled oscillators (VCOs) [8]. DDS provides precise phase coherence through digital waveform synthesis but suffers from poor phase noise and spurious signals at high frequencies. PLLs synchronize multiple oscillators to a common reference but are limited by feedback loop bandwidth and noise. VCOs generate tunable signals through voltage control, achieving dual-band signals via mixing or frequency multiplication, yet their high phase noise restricts precision at higher frequencies. As a result of well-known electronic limitations, microwave pulse signals generated using these components face challenges in expanding to multiple high-frequency bands, with their phase noise performance degrading significantly as the frequency increases. [9]. These limitations have prompted the pursuit of microwave photonic techniques as viable alternatives.

Optoelectronic oscillators (OEOs) [10], [11], which incorporate long optical delay lines, have become attractive candidates for generating high-frequency microwave signals with ultralow phase noise. Over the past decade, significant advancements have been made in phase noise suppression [12], [13], [14], sidemode suppression [15], [16], [17], wideband waveform generation [18], [19], signal processing [20], [21] and so on. However, conventional single-loop OEOs inherently support only one oscillation mode due to intracavity mode competition, making multiband signal generation challenging [22], [23].

Inspired by the topological similarity between OEOs and mode-locked lasers, mode-locking techniques have been adapted to OEOs to enable microwave pulse generation. In [24], a passive mode-locking scheme was demonstrated by saturating the in-loop high-frequency amplifier, producing single-band microwave pulses at a carrier frequency of 650 MHz with a repetition rate of 1.0543 MHz. In [25], [26], [27], [28], and [29], active mode-locking has been implemented in OEOs, where an external low-frequency signal is introduced to dynamically control the gain within the loop cavity. This

Received 20 May 2025; revised 2 August 2025 and 28 September 2025; accepted 30 September 2025. This work was supported in part by the National Key Research and Development Program of China under Grant 2022YFB2802704, in part by Jiangsu Funding Program for Excellent Postdoctoral Talent under Grant 2022ZB237, and in part by the National Natural Science Foundation of China under Grant 62271249 and Grant 62071226. *(Corresponding author: Shifeng Liu.)*

Changlong Du, Shifeng Liu, Li Yang, Mingzhen Liu, Liangzun Tang, and Shilong Pan are with the National Key Laboratory of Microwave Photonics, Nanjing University of Aeronautics and Astronautics, Nanjing 210016, China (e-mail: changlongdu@nuaa.edu.cn; sfliu_nuaa@nuaa.edu.cn; liyang_photonic@nuaa.edu.cn; liumingzhen@nuaa.edu.cn; lztang@nuaa.edu.cn; pans@nuaa.edu.cn).

Hao Chen is with Hangzhou Institute of Advanced Studies, Zhejiang Normal University, Hangzhou 311231, China.

Digital Object Identifier 10.1109/TMTT.2025.3620573

approach facilitates phase-locking among adjacent oscillation modes, leading to the successful generation of microwave pulse signals. By adjusting the frequency of the modulation signal to match an integer multiple of the free spectral range (FSR) of the active mode-locking OEO (AML-OEO), phase coherence among longitudinal modes is established, allowing stable multimode oscillation. Additionally, pulse repetition frequency of the generated pulses can be tuned using harmonic mode-locking technology. While most reported mode-locked OEOs focus on single-band operation, dual-band microwave pulse generation has also been explored in OEOs [28], [29]. In [28], a polarization-multiplexed active mode-locking OEO employing a dual-polarization binary phase shift keying modulator was demonstrated for the generation of frequency-tunable dual-band microwave pulses; however, the two pulse trains were phase-independent and thus lacked coherence, and the generated signals were prone to degraded amplitude and frequency stability due to polarization variations induced by environmental perturbations. In [29], an OEO employing an ASE source, a programmable optical filter, and long fiber dispersion achieved single-frequency, dual-frequency, and mode-locking oscillations, but the generated signals exhibited relatively poor phase noise and signal-to-noise ratio, lacked mutual coherence, and the overall configuration was relatively complicated.

In this work, we propose and experimentally demonstrate a novel approach for generating coherent dual-band microwave pulse signals based on an AML-OEO. In the proposed scheme, the carrier frequencies of the dual-band signals are determined by a dual-band bandpass filter (DB-BPF) incorporated into the OEO loop. An external RF signal, with a frequency equal to the difference between the two oscillation frequencies, is injected into the loop to establish phase coherence between the two oscillation tones. Leveraging the nonlinearity of the Mach–Zehnder modulator (MZM), this injection induces mutual frequency conversion and energy coupling between the two carriers, thereby synchronizing their phases. To achieve active mode-locking, an external single-tone electrical signal with a frequency that is an integer multiple of the FSR of the loop is applied to the bias ports of the MZM, dynamically modulating the loop gain. This modulation enables phase locking among adjacent longitudinal modes, resulting in the generation of microwave pulse signals with a repetition frequency equal to that of the injected low-frequency signal. Moreover, by injecting a custom-designed full-wave signal, dual-band staggered double-pulse waveforms can be produced within a single cavity round-trip time. The phase coherence of the dual-band microwave pulse signals is preserved through intracavity mutual injection locking. This architecture opens a new pathway toward waveform generation for advanced dual-band radar and communication applications.

II. Principle and Analysis

Fig. 1(a) depicts the principle of generating coherent dual-band microwave pulse generation using an AML-OEO [22]. The continuous-wave light from the laser diode is passed through a variable attenuator and then fed into the MZM, where it is modulated by the feedback microwave signal, resulting in an intensity-modulated optical waveform. After passing through the single-mode fiber, the modulated optical signal is converted to a photocurrent by the high-speed photodetector (PD). The electrical signal generated by the PD passed through a DB-BPF, which selects the desired oscillation frequencies for the OEO. An electrical amplifier is subsequently employed to compensate for loop losses. After that, the electrical signal is split into two paths by an electrical coupler. One path is directed to a phase noise analyzer for phase noise performance and frequency spectrum measurement, while the other is fed back into the MZM with an external RF signal by another electrical coupler to complete the OEO loop. Unlike traditional OEOs, the bias ports of the MZM are driven by low-frequency electrical waveform from an arbitrary waveform generator (AWG) rather than a direct-current (dc) voltage. Adjusting the amplitude and frequency of the low-frequency electrical waveform allows dynamic tuning of the cavity's net gain, thereby facilitating the formation of microwave pulse signals. When the AWG is switched off and the RF source is activated, the OEO operates in a dual-frequency oscillation mode, producing coherent dual-frequency signals. The two oscillation modes are selected by the DB-BPF with the center frequencies denoted ω_1 and ω_2. An external RF signal, produced by a signal generator

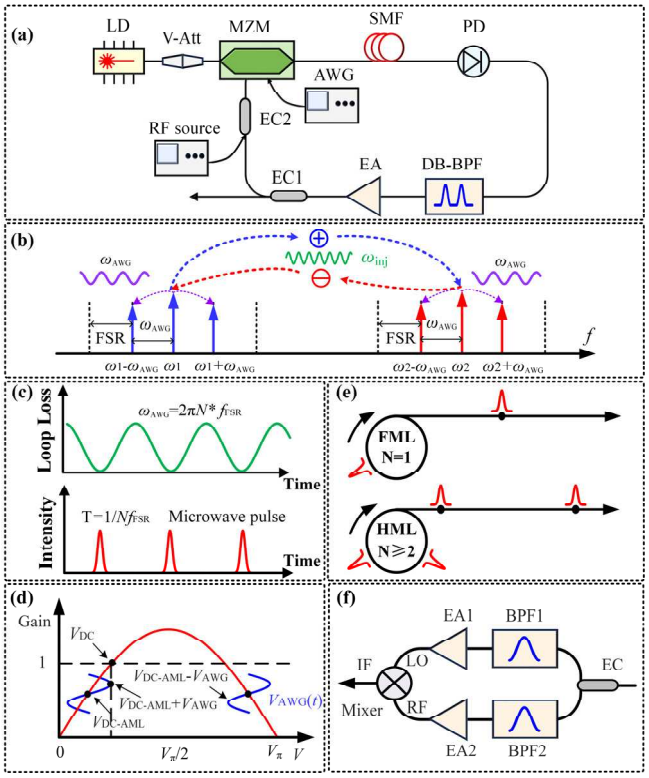

Fig. 1. Principle of microwave pulse signals generation based on an actively mode-locked OEO. (a) Schematic of the experimental setup. (b) Frequency relationships between the injection frequency and the two oscillation frequencies. (c) Time domain mechanism of AML-OEO mechanism. (d) Generation of dual-band phase-coherent pulse signals by bias-controlled modulation of loop gain. (e) Generation of microwave pulses under fundamental ($N = 1$) and harmonic ($N \geq 2$) mode locking. (f) Setup for verifying the phase coherence of the dual-frequency signal through frequency down-conversion. LD: laser diode, V-Att: variable attenuator, MZM: Mach–Zehnder modulator, SMF: single-mode fiber, PD: photodetector, DB-BPF: dual-band bandpass filter, EA: electrical amplifier, EC: electrical coupler, AWG: arbitrary waveform generator, and FSR: free spectral range.

and corresponding to the frequency spacing between the two oscillation signals, is introduced into the OEO loop. In the steady state, the frequency of the injection signal ω_{inj} equals $\omega_2 - \omega_1$. As depicted in Fig. 1(b), frequency mixing occurs in the MZM due to its modulation nonlinearity. During the frequency mixing process, the oscillation frequency of ω_2 is downconverted to $\omega_2 - \omega_{\text{inj}}$ by mixing with ω_{inj}. As ω_{inj} equals $\omega_2 - \omega_1$ in the steady state, the downconverted frequency equals ω_1 and is injected into the ω_1 oscillation loop. By carefully adjusting the loop gain and phase, the oscillation loop at ω_1 is injection-locked by the downconverted signal from ω_2. Simultaneously, the oscillation frequency of ω_1 is upconverted to $\omega_1 + \omega_{\text{inj}}$, which then injection locks the oscillation loop at ω_2 using a similar mechanism. This process achieves mutual injection locking between the two oscillation modes and suppresses loop gain competition. Consequently, two stable and coherent frequencies oscillate in a single OEO loop [22].

The voltage expression of the microwave signal applied to the MZM can be mathematically described as follows:

$$V_{\text{in-MZM}}(t) = V_{\text{inj}} \cos\left(\omega_{\text{inj}} t + \varphi_{\text{inj}}\right) + V_1 \cos\left(\omega_1 t + \varphi_1\right) + V_2 \cos\left(\omega_2 t + \varphi_2\right) \quad (1)$$

where $V_{\text{inj}}, V_1, V_2, \varphi_{\text{inj}}, \varphi_1, \varphi_2$ are the electrical amplitude and initial phase of the injection signal and the two oscillation signals, respectively. Introducing $V_{\text{in-MZM}}(t)$ to the transmission function of the MZM, the signal after a single round-trip in the OEO loop, which is reinjected into the MZM, can be written as [10]

$$V_{\text{EA}}(t) = V_{\text{ph}} \left\{1 + \cos \pi \left[V_{\text{in-MZM}}(t)/V_\pi + V_{\text{DC}}/V_\pi\right]\right\} \quad (2)$$

where $V_{\text{ph}} = 0.5\alpha_0 G_A R \Re P_c \exp(-\alpha L), \alpha_0$ is the insertion loss of the modulator, G_A represents the voltage gain of the electrical amplifier, R and $\Re$ denote the impedance and responsivity of the PD, respectively; P_c is the optical power injected into the MZM; α and L are the attenuation coefficient and the length of the single-mode fiber, respectively. V_{dc} is applied dc bias voltage, and V_π is half-wave voltage of the MZM. Additionally, assuming small-signal modulation in oscillation loop, the DB-BPF filters out high-order harmonics and other intermodulated frequency components. Therefore, the final output signal, after being filtered by the DB-BPF, is given by

$$\begin{aligned} V_{\text{out-BPF}}(t) \propto V_{\text{ph}} \Bigg\{ & J_0\left(\frac{\pi V_2}{V_\pi}\right) J_0\left(\frac{\pi V_{\text{inj}}}{V_\pi}\right) J_1\left(\frac{\pi V_1}{V_\pi}\right) \sin\left(\frac{\pi V_{\text{DC}}}{V_\pi}\right) \cos\left(\omega_1 t + \varphi_1\right) \\ & + J_0\left(\frac{\pi V_{\text{inj}}}{V_\pi}\right) J_0\left(\frac{\pi V_1}{V_\pi}\right) J_1\left(\frac{\pi V_2}{V_\pi}\right) \sin\left(\frac{\pi V_{\text{DC}}}{V_\pi}\right) \cos\left(\omega_2 t + \varphi_2\right) \\ & - J_0\left(\frac{\pi V_2}{V_\pi}\right) J_1\left(\frac{\pi V_{\text{inj}}}{V_\pi}\right) J_1\left(\frac{\pi V_1}{V_\pi}\right) \cos\left(\frac{\pi V_{\text{DC}}}{V_\pi}\right) \cos\left[\left(\omega_1 + \omega_{\text{inj}}\right) t + \varphi_1 + \varphi_{\text{inj}}\right] \\ & - J_0\left(\frac{\pi V_1}{V_\pi}\right) J_1\left(\frac{\pi V_{\text{inj}}}{V_\pi}\right) J_1\left(\frac{\pi V_2}{V_\pi}\right) \cos\left(\frac{\pi V_{\text{DC}}}{V_\pi}\right) \cos\left[\left(\omega_2 - \omega_{\text{inj}}\right) t + \varphi_2 - \varphi_{\text{inj}}\right] \Bigg\} \end{aligned} \quad (3)$$

where $J_n(^*)$ is the nth Bessel function, and according to (3), in order to introduce intermodulation terms between the dual-frequency signal and the external injection signal, the MZM must not operate at the quadrature bias point, that is, $V_{\text{dc}} \neq V_\pi/2$. As shown in (3), the output signal comprises the oscillation frequencies ω_1 and ω_2, as well as frequency-converted components $\omega_1 + \omega_{\text{inj}}$ and $\omega_2 - \omega_{\text{inj}}$, which arise from the nonlinear characteristics of the MZM. When the injection signal at ω_{inj} is set equal to the difference between ω_1 and ω_2, the down-converted component $\omega_2 - \omega_{\text{inj}}$ coincides with ω_1, thereby injection-locking the mode at ω_1. Simultaneously, the upconverted component $\omega_1 + \omega_{\text{inj}}$ injection-locks the mode at ω_2. The single-tone microwave signals at f_1 and f_2 have phases locked to $\varphi_2 - \varphi_{\text{inj}}$ and $\varphi_1 + \varphi_{\text{inj}}$, respectively, establishing a stable phase synchronization. These frequency conversion and mutual injection-locking processes suppress mode competition, enable stable dual-frequency oscillation, and maintain a fixed phase relationship, resulting in strongly phase-coherent dual-frequency oscillation.

When the AWG is turned on, active mode-locking is initiated within the loop, causing all longitudinal modes within each filter passband to become phase-locked. In the time domain, a periodic electrical signal is applied to the bias port of the MZM, resulting in a periodic modulation of the net gain in the OEO loop. Mathematically, the microwave signal driving the MZM bias port can be expressed as

$$V_{\text{AWG}}(t) = V_{\text{AWG}} \sin\left(\omega_{\text{AWG}} t\right) \quad (4)$$

where V_{AWG}, and ω_{AWG} are the electrical amplitude and angular frequency of the low-frequency electrical waveform. The frequency of the low-frequency electrical waveform will meet

$$\omega_{\text{AWG}} = 2\pi N f_{\text{FSR}} \quad (5)$$

where N is positive integer, and the corresponding output optical signal of the MZM can be expressed as follows:

$$\begin{aligned} E_{\text{out}} &= E_0 \exp\left(j\omega_c t\right) \cos\left(\frac{\pi}{V_\pi} V_{\text{in}}(t) + \frac{\pi}{V_\pi} V_{\text{bias}}(t)\right) \\ &= E_0 \exp\left(j\omega_c t\right) \cos\left(\frac{\pi}{V_\pi} V_{\text{in}}(t) + \frac{\pi V_{\text{DC-AML}}}{V_\pi} + \frac{\pi V_{\text{AWG}}}{V_\pi} \sin\left(\omega_{\text{AWG}} t\right)\right) \end{aligned} \quad (6)$$

where E_0 represents the amplitude and ω_c denotes the angular frequency of the optical carrier. $V_{\text{bias}}(t) = V_{\text{dc-AML}} + V_{\text{AWG}} \sin(\omega_{\text{AWG}} t)$ is the bias voltage of the MZM, where $V_{\text{dc-AML}}$ is the applied dc bias voltage under the AML state. $V_{\text{in}}(t)$ is the oscillation signal in the loop.

Following a single cavity loop, the electrical signal applied to the MZM can be described by:

$$V_{\text{out}}(t) = V_{\text{ph}} \left\{1 + \cos\left[\frac{\pi}{V_\pi} V_{\text{in}}(t) + \frac{\pi V_{\text{DC-AML}}}{V_\pi} + \frac{\pi V_{\text{AWG}}}{V_\pi} \sin\left(\omega_{\text{AWG}} t\right)\right]\right\}. \quad (7)$$

Thus, the open-loop small-signal gain of the OEO in the time domain is calculated is [24]

$$G_{\text{s}}(t) = \left.\frac{dV_{\text{out}}}{dV_{\text{in}}}\right|_{V_{\text{in}}=0}$$

$$= \left| -\frac{\pi V_{\text{ph}}}{V_\pi} \sin\left[\frac{\pi V_{\text{DC-AML}}}{V_\pi} + \frac{\pi V_{\text{AWG}}}{V_\pi} \sin\left(\omega_{\text{AWG}} t\right) \right] \right|. \tag{8}$$

According to (8), the small-signal gain $G_s(t)$ of the open-loop is governed by the bias voltage of the MZM. This results in a time-varying modulation of the loop gain, with a modulation frequency equal to that of the externally applied low-frequency electrical waveform. When this driving signal is a periodic sinusoidal waveform, the corresponding temporal variation in loss within the OEO loop is depicted in Fig. 1(c). The loop oscillation occurs when the loop reaches its minimum loss. At these moments, the net loop gain exceeds unity, allowing microwave signals to be amplified during each round-trip. According to (3), when the MZM is biased at V_{dc}, coherent dual-frequency signals are generated in the OEO through mutual energy coupling and frequency conversion, effectively breaking the intracavity gain competition. Under this condition, the variable attenuator is adjusted to ensure that the loop gain at the dual-frequency operating point is slightly greater than one, thereby just meeting the oscillation threshold. As described by (8), the loop gain is dynamically modulated by the externally applied low-frequency driving signal. To fulfill the oscillation condition, namely that the loop gain exceeds unity, the instantaneous bias must satisfy

$$V_{\text{DC-AML}} \pm V_{\text{AWG}} = V_{\text{DC}}. \tag{9}$$

As shown in Fig. 1(d), when the dc bias used for generating dual-frequency signals is set below the quadrature point ($V_{\text{dc}} < V_\pi/2$), the oscillation condition [as described by (9)] is satisfied only when the sum of the dc bias $V_{\text{dc-AML}}$ and the amplitude of the modulation signal V_{AWG} equals the bias voltage required for generating coherent dual-frequency signals V_{dc}. At this moment, the loop gain slightly exceeds unity, triggering oscillation and enabling the generation of dual-frequency signals. This means that oscillation occurs only when the driving waveform reaches its peak amplitude, at which point the loop gain exceeds unity and coherent dual-frequency oscillation is initiated. At all other times, the loop gain remains below unity, and oscillation is suppressed. If $V_{\text{dc-AML}} + V_{\text{AWG}} > V_{\text{dc}}$, the oscillation condition is still satisfied, and microwave signals can be generated. However, this leads to an extended duration during which the loop gain remains above unity, resulting in wider output pulses. More critically, the effective bias point deviates from the condition defined by (3), thereby disrupting the generation of coherent dual-frequency oscillations. Similarly, as shown in Fig. 1(d), when the dc bias used to generate the dual-frequency signal is set below the quadrature point, the sum of the dc bias $V_{\text{dc-AML}}$ and the modulation amplitude V_{AWG} must satisfy $V_{\text{dc-AML}} - V_{\text{AWG}} = V_{\text{dc}}$. Under these conditions, the OEO establishes active mode-locking, generating microwave pulses with a carrier frequency equal to the center frequency of the DB-BPF and a repetition rate matching the modulation frequency. In the frequency domain, this corresponds to equally spaced, phase-coherent longitudinal modes. As shown in Fig. 1(e) and described by (8), when $N = 1$, the system operates under fundamental mode-locking with one pulse per round-trip; when $N > 1$, harmonic mode-locking occurs, producing N pulses per round-trip.

Since the dual-frequency signals propagate within the same OEO loop, they experience identical dynamic gain modulation. By applying a common amplitude modulation to the phase-coherent dual-frequency carriers, dual-band microwave pulse signals are generated in the time domain. In the frequency domain, each band exhibits evenly spaced and phase-locked oscillation modes, enabling coherent multimode oscillation. Owing to the mutual phase locking between the two carriers, the resulting frequency combs in both bands inherit mutual coherence. Through the transitivity of coherence, all spectral components within and across the two bands maintain a stable phase relationship, leading to strongly phase-coherent dual-band pulse waveforms.

III. Experimental Results

A proof-of-concept experiment was conducted using the configuration depicted in Fig. 1(a). A narrow-linewidth laser diode (EM650) provides 20 dBm optical power centered at 1550.2 nm. The MZM (Fujitsu FTM7938) features an RF bandwidth exceeding 20 GHz and a half-wave voltage (V_π) of 5 V. The 2-km single-mode fiber introduces approximately 1 dB of transmission loss. The high-speed photodiode (CETC44 GD45220R) has an RF bandwidth of 20 GHz and a responsivity of 0.8 A/W. The low-noise electrical amplifier (Talent Microwave TLNA02G18G) provides an RF gain of 30 dB from 2 to 18 GHz. The DB-BPF has two passbands centered at 10 and 16.08 GHz, with 3-dB bandwidths of 10 and 20 MHz, respectively. A microwave signal generator is employed to produce the external injection signal (Keysight E8257D), and the spectral characteristics of the generated RF signals are analyzed using a phase noise analyzer (R&S FSWP26) with spectrum analysis capabilities. When the AWG is turned off and the RF source is turned on, a stable dual-frequency signal can be generated by tuning the MZM bias voltage and adjusting the phase shifter in the loop.

Fig. 2 exhibits measured spectrum of the generated dual-frequency microwave signals. As shown in Fig. 2(a), two distinct microwave tones are simultaneously generated at 10 GHz (X-band) and 16.091 GHz (Ku band), precisely aligned with the center frequencies of the DB-BPF. The measured output powers of the two signals are 0.2 and 0.1 dBm, respectively. According to the injection-locked OEO phase noise model [30], the near-carrier phase noise of the generated signal primarily follows that of the injection source, while the far-from-carrier phase noise is determined by the free-running OEO. A stronger injection power can extend the influence of the injection source across a broader offset range, and the MZM bias point simultaneously affects the loop gain and the phase noise of the free-running component. As a result, the phase noise characteristics of the generated dual-frequency signals vary with different combinations of injection power [23] and MZM bias. In our experiment, the injected signal was set to 6.091 GHz, precisely matching the separation between the two oscillation modes, with an injection power of 5 dBm. The dc bias voltage of the MZM was adjusted to 4.8 V, about 1 V below the quadrature point of 5.8 V. This specific combination of injection power and bias voltage effectively broke the mode competition and yielded optimal performance in terms of both side-mode suppression ratio and phase noise. The primary spurious component observed is the second harmonic of the

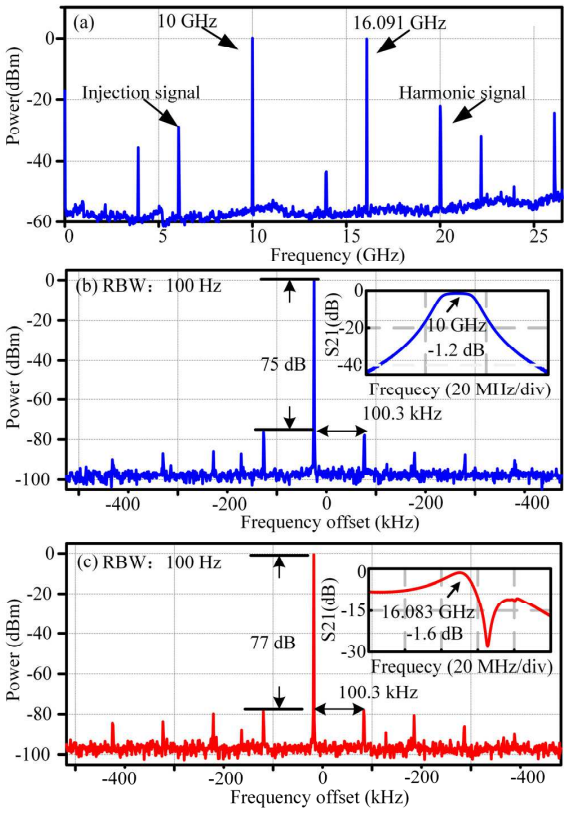

Fig. 2. (a) Measured spectrum of the generated dual-frequency microwave signals over a 26.5 GHz span. (b) Detailed spectrum of the 10 GHz signal within a 1 MHz span. (c) Detailed spectrum of the 16.091 GHz signal within a 1 MHz span. RBW: resolution bandwidth.

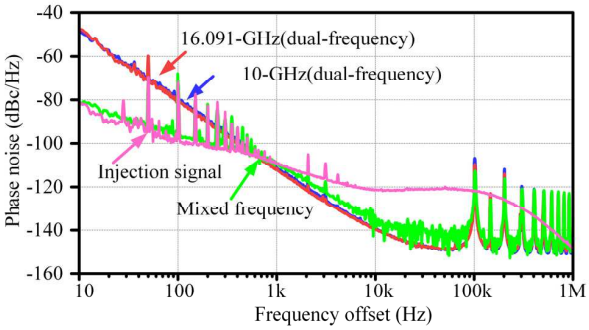

Fig. 3. Single-sideband phase noise curves of the generated dual-frequency microwave signal when AWG is turned off.

10 GHz tone, while other spurious signals arise from nonlinear mixing effects within the MZM and electrical amplifiers, as well as residual leakage of the injected signal. Fig. 2(b) and (c) provides zoomed-in view views of the 10 and 16.091 GHz signals over a 1 MHz span, shown as the blue and red traces, respectively. Insets in both figures display the corresponding S21 transmission responses of the DB-BPF, confirming the precise spectral alignment of the generated tones. A side-mode suppression ratio exceeding 75 dB is observed for both signals, validating the effectiveness of injection-locking. Both signals exhibit a FSR of 100.3 kHz, serving as a critical reference for determining the suitable driving frequency used in active mode-locking and gain modulation.

The single-sideband phase noise spectra of the generated RF signals are shown in Fig. 3. The blue and red

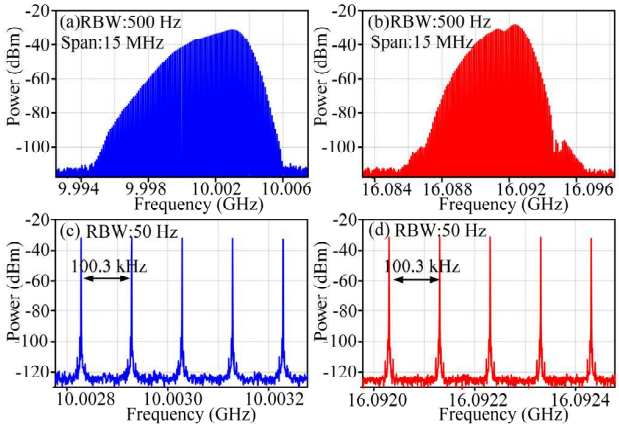

Fig. 4. Measured spectra of the generated dual-band microwave signals. (a) Spectrum in the X–band. (b) Spectrum in the Ku band. (c) Magnified view of (a) within a 500 kHz span. (d) Magnified view of (b) within a 500 kHz span.

traces represent the phase noise of the 10 and 16.091 GHz tones, respectively. Both frequency components display similar low phase noise characteristics, with values better than −139 dBc/Hz at a 10 kHz frequency offset. To further evaluate their phase coherence, the generated dual-frequency signal is divided into two paths using an electrical coupler, as shown in Fig. 1(f). The 10 and 16 GHz components are first isolated using narrowband bandpass filters, and each filtered signal is then amplified by a low-noise amplifier (TLPNA0.1G22G-12-18) to provide sufficient power for driving the mixer. The two signals are fed into the LO and RF ports of a mixer (Marki T218GLS), respectively. The down-converted signal is subsequently sent to an FSWP for phase noise measurement. The resulting difference-frequency signal exhibits a 30 dB reduction in phase noise at a 10 Hz offset, compared to either individual tone, confirming excellent coherence and mutual stability. It is worth noting that the slightly higher phase noise observed in the mixed signal beyond 1 kHz offset, compared to that of the original dual-frequency OEO output, is primarily attributed to the additive phase noise introduced during the downconversion process [31], [32], [33], which arises from the combined effects of the nonideal noise characteristics of the low-noise amplifiers preceding the mixer and the intrinsic noise contributions of the mixer itself.

By setting the dc bias of the MZM to 4.6 V ($V_{\mathrm{dc-AML}}$), activating the AWG, and applying an external modulation signal with a frequency of 100.3 kHz (matching the FSR of the OEO) and an amplitude of 0.2 V, and by adjusting the variable attenuator, the longitudinal modes within the loop become phase-locked, thereby achieving fundamental mode-locking. As a result, all longitudinal modes that fall within the net gain bandwidth, which is primarily determined by the DB-BPF, oscillate simultaneously, as illustrated in Fig. 4. This observation confirms coherent multimode oscillation within the OEO loop and demonstrates that gain competition has been effectively mitigated through the active mode-locking mechanism. Fig. 4(a) and (b) shows the measured RF spectra for the generated signals at 10 GHz (X-band, blue) and 16.091 GHz (Ku band, red), respectively. The 3-dB spectral bandwidths are constrained by the narrow passbands of the employed electronic filters. The difference in spectral envelopes between

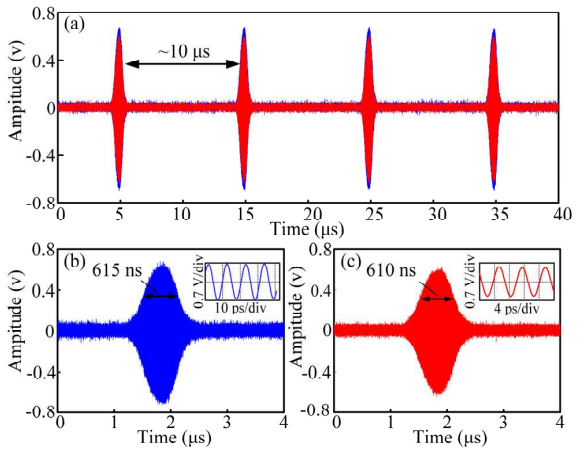

Fig. 5. Measured temporal waveforms of the generated dual band microwave pulse signals in the fundamental mode-locking state. (a) Overall pulse train with a 10-μs period. (b) X-band (10 GHz) pulse with a 615-ns width. (c) Ku-band (16.091 GHz) pulse with a 610-ns width.

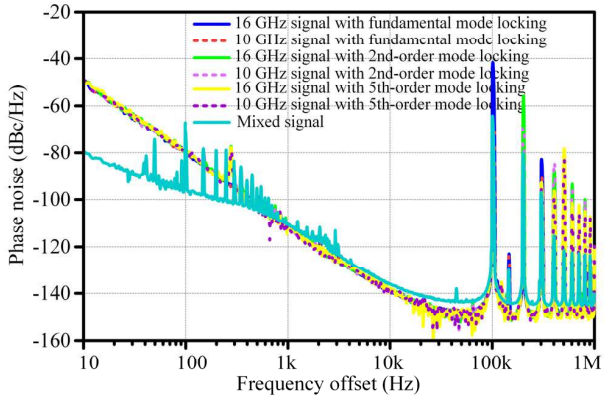

Fig. 6. Single-sideband phase noise of the generated microwave pulse signals centered at 10 and 16.091 GHz.

the two bands arises from the distinct filtering characteristics of the DB-BPF. A zoomed-in view of the spectrum over a 500 kHz span reveals a longitudinal mode spacing of 100.3 kHz, confirming operation under fundamental mode-locking. The measured signal-to-noise ratio exceeds 90 dB, indicating high spectral purity, which can be attributed to the high Q-factor of the OEO loop.

After filtering, the dual-band pulse signals are routed to two separate channels of a real-time oscilloscope. Fig. 5 presents the measured time-domain waveform of the generated dual-band microwave pulse train under fundamental mode-locking. The blue trace corresponds to the pulse signal centered at 10 GHz, whereas the red trace represents the signal at 16.091 GHz. Both waveforms share nearly identical amplitude envelopes and exhibit a repetition period of approximately 10 μs, corresponding to a pulse repetition frequency of 100.3 kHz. The full width at half-maximum of the microwave pulse signals in the X-band and Ku band are 615 and 610 ns, respectively. A zoomed-in view of the oscillation within a single microwave pulse reveals center frequencies of approximately 10 and 16.091 GHz, respectively. The temporal waveforms of the dual-band microwave pulse signals exhibit significant overlap, indicating synchronization in the time domain and identical temporal sequences.

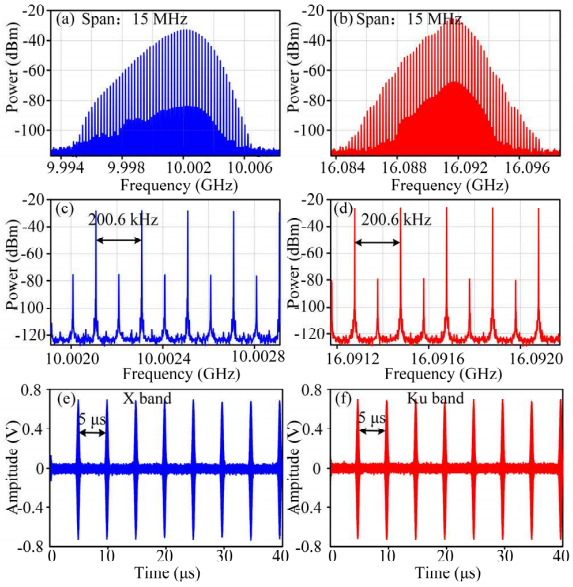

Fig. 7. Measured spectra and temporal waveforms of the generated microwave pulse signals under second-order harmonic mode locking. (a) Spectrum of the X-band signal. (b) Spectrum of the Ku-band signal. (c) Magnified view of (a) showing a mode spacing of 200.6 kHz. (d) Magnified view of (b) showing a mode spacing of 200.6 kHz. (e) Time-domain waveform of the X-band pulse train with a 5-μs period. (f) Time-domain waveform of the Ku-band pulse train with a 5-μs period.

Fig. 6 illustrates the single-sideband phase noise of the generated dual-band microwave pulse signals at 10 GHz (red dashed line) and 16.091 GHz (blue solid line) from an AML-OEO. The oscillating signals in both bands show comparable phase noise characteristics. At a 1-kHz frequency offset, the phase noise is better than -112 dBc/Hz, and at a 10-kHz frequency offset, it is better than -139 dBc/Hz. In Doppler radar systems, low-phase noise microwave pulse signals improve the accuracy and sensitivity of velocity measurements. To verify the coherence of the dual-band microwave pulse signals, the two outputs are filtered and mixed using a frequency mixer after amplification. The resulting difference-frequency signal exhibits a 30 dB phase noise improvement at a 10 Hz offset compared to individual signals, as shown by the light green curve in Fig. 6. This result confirms the high phase and frequency coherence between the two bands, attributed to the mutual injection locking mechanism.

Microwave pulse signals with tunable pulse repetition frequency are highly desirable in modern radar applications, as they enhance velocity resolution, improve resistance to jamming, and offer increased operational flexibility. However, in conventional OEO, the fixed length of optical fibers inherently restricts the loop's FSR, thus limiting pulse repetition frequency agility. Although replacing fibers of different lengths can overcome this constraint, it introduces additional system complexity and redundancy. To overcome this limitation, harmonic mode-locking is adopted by setting the modulation frequency to an integer multiple of the cavity's FSR. Fig. 7 illustrates the spectra and temporal waveform for second harmonic mode-locking, achieved by setting the frequency of the low-frequency electrical waveform to 200.6 kHz. The RF spectra in Fig. 7(a) and (b), measured with a RBW of 500 Hz, show stable multimode oscillations centered at 10 and 16.091 GHz. The zoomed-in spectra over a

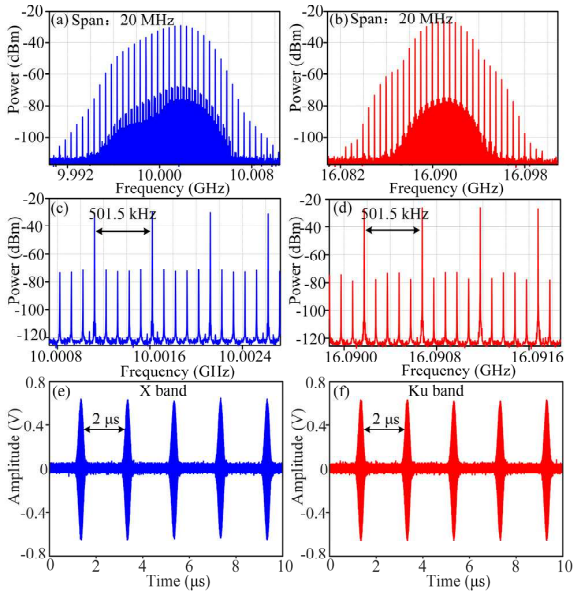

Fig. 8. Measured spectra and temporal waveforms of the generated microwave pulse signals under fifth-order harmonic mode locking. (a) Spectrum of the X-band signal. (b) Spectrum of the Ku-band signal. (c) Magnified view of (a) showing a mode spacing of 501.5 kHz. (d) Magnified view of (b) showing a mode spacing of 501.5 kHz. (e) Time-domain waveform of the X-band pulse train with a 2-μs period. (f) Time-domain waveform of the Ku-band pulse train with a 2-μs period.

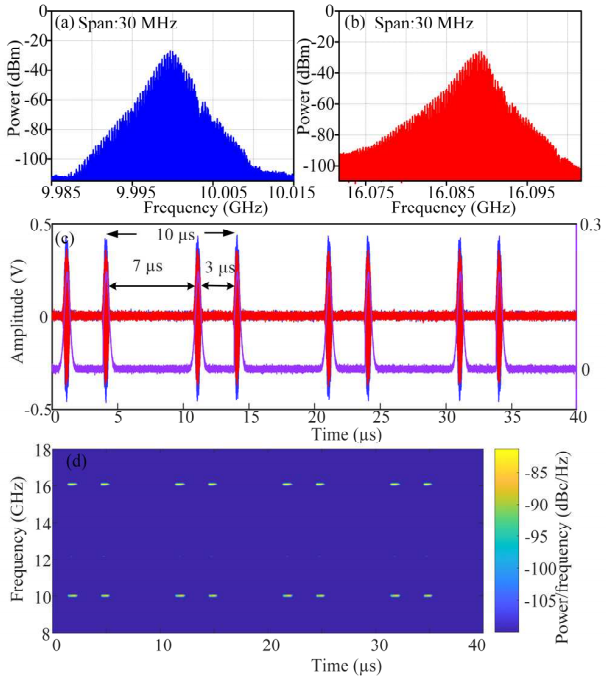

Fig. 9. Spectra of the generated staggered double-pulse signals at (a) 10 GHz and (b) 16.091 GHz. (c) Temporal waveforms of the X-band (blue) and Ku-band (red) pulse signals, along with the injected waveform (purple). (d) Spectrogram of the dual-band staggered double-pulse signals.

1 MHz span in Fig. 7(c) and (d) reveal a longitudinal mode spacing of 200.6 kHz, confirming second harmonic mode-locking ($N = 2$). The corresponding time-domain signals in Fig. 7(e) and (f) exhibit pulse periods of ~5 μs, consistent with the doubled pulse repetition frequency. Nevertheless, spurious supermodes with the same interval of 200.6 kHz are observed between the dominant comb lines, with a suppression ratio of approximately 43 dB, as indicated in Fig. 7(c) and (d). These supermodes, lacking phase coherence, degrade pulse quality, and power stability. Numerous techniques have been proposed to suppress such supermode noise in AML-OEO systems [34], [35]. Fig. 8 demonstrates the results under fifth-harmonic mode-locking, where the modulation frequency is set to 501.5 kHz, increasing the mode spacing and reducing the pulse period to ~2 μs. Despite the increased pulse repetition frequency, the measured phase noise remains consistent across different harmonic orders, as shown in Fig. 6. This demonstrates the robustness of the proposed scheme in generating high-repetition-rate microwave pulse signals with excellent phase noise performance, making it well-suited for high-resolution radar and high-data-rate communication systems.

Conventional pulse trains with fixed pulse repetition frequency inherently limit the trade-off between maximum unambiguous range and maximum unambiguous velocity in radar systems [36]. In contrast, staggered pulse waveforms, characterized by nonuniform time intervals between adjacent pulses, offer a promising solution to this constraint [37], [38]. By varying the pulse time interval according to predefined patterns, these waveforms enable a significant enhancement in the maximum unambiguous velocity—albeit with a slight compromise in range resolution. In our experiment, the AWG is configured to output a waveform with a total period of 10 μs, containing two Gaussian-shaped pulses with unequal temporal spacing within each cycle, as illustrated by the purple curve in Fig. 9(c). In this configuration, during a single-loop period, the loop gain exceeds unity at two distinct moments. According to (8), the OEO oscillates at these specific moments, resulting in the generation of staggered pulse signals at the corresponding positions. Fig. 9(a) and (b) displays the spectra of the staggered double-pulse signals with carrier frequencies of 10 and 16.091 GHz, respectively. The corresponding time-domain waveforms are presented in Fig. 9(c), where the blue and red curves represent the X-band and Ku-band signals. The temporal spacing between the two pulses exhibits a 7:3 ratio, which aligns well with the injected waveform, validating the control strategy and corroborating theoretical expectations. To analyze the time–frequency characteristics of the generated waveform, the output signals from the OEO are directly captured by a real-time oscilloscope and processed using a short-time Fourier transform. The resulting spectrogram is shown in Fig. 9(d). The time–frequency plot clearly confirms the generation of dual-band staggered double-pulse signals, simultaneously centered at 10 and 16.091 GHz.

IV. Conclusion

In this article, we proposed and experimentally demonstrated a novel method for generating coherent dual-band microwave pulse signals based on an AML-OEO. The carrier frequencies of the dual-band signals are selected using a DB-BPF inserted in the OEO loop. Phase coherence between the two oscillation modes is established by injecting a radio frequency signal whose frequency equals the difference between the two oscillating tones. This injection induces nonlinear frequency conversion and energy exchange through the MZM, enabling mutual injection locking and thereby stabilizing

phase-coherent dual-frequency oscillation. To realize pulse signal generation, a low-frequency electrical waveform is applied to the MZM bias port, dynamically modulating the loop gain. By dynamically modulating the gain, the phases of neighboring longitudinal modes are synchronized, thereby establishing coherence among all oscillation modes within the cavity's net gain bandwidth. As a result, coherent dual-band microwave pulse trains are generated via the temporal superposition of longitudinally phase-locked modes centered at the two oscillation frequencies. The generated pulses maintain phase coherence in both the time and frequency domains. In a proof-of-concept experiment, dual-band microwave pulse signals centered at 10 and 16.091 GHz were successfully generated. Pulse repetition frequencies of 100.3, 200.6, and 501.5 kHz were achieved under fundamental and harmonic mode-locking regimes. Furthermore, by injecting a custom-designed modulation signal, staggered double-pulse waveforms were obtained within a single cavity period. The phase noise of the generated microwave pulse signal was measured to be below −139 dBc/Hz at a 10 kHz offset frequency. The proposed scheme offers a compact, flexible, and high-performance solution for the generation of phase-coherent microwave waveforms, making it highly promising for applications in pulse radar, advanced wireless communication, and electronic warfare systems.

REFERENCES

[1] S. Peng, S. Li, X. Xue, X. Xiao, D. Wu, and X. Zheng, "A photonics-based coherent dual-band radar for super-resolution range profile," *IEEE Photon. J.*, vol. 11, no. 4, pp. 1–8, Aug. 2019.

[2] T. H. Brandão et al., "Coherent dual-band radar system based on a unique antenna and a photonics-based transceiver," *IET Radar, Sonar Navigat.*, vol. 13, no. 4, pp. 505–511, Apr. 2019.

[3] M. Parker, *Digital Signal Processing 101: Everything You Need To Know To Get Started*. Oxford, U.K.: Newnes, 2017.

[4] F. Scotti, F. Laghezza, P. Ghelfi, and A. Bogoni, "Multi-band software-defined coherent radar based on a single photonic transceiver," *IEEE Trans. Microw. Theory Techn.*, vol. 63, no. 2, pp. 546–552, Feb. 2015.

[5] J. Shi, F. Zhang, X. Ye, Y. Yang, D. Ben, and S. Pan, "Photonics-based dual-functional system for simultaneous high-resolution radar imaging and fast frequency measurement," *Opt. Lett.*, vol. 44, no. 8, pp. 1948–1951, Apr. 2019.

[6] Q. Li, D. Yang, X. H. Mu, and Q. L. Huo, "Design of the L-band wideband LFM signal generator based on DDS and frequency multiplication," in *Proc. Int. Conf. Microw. Millim. Wave Technol. (ICMMT)*, vol. 4, Shenzhen, China, May 2012, pp. 1–4.

[7] Y.-K. Tsai, Y.-K. Hsieh, H.-Y. Tsai, H.-S. Chen, and L.-H. Lu, "A concurrent dual-band and dual-mode frequency synthesizer for radar systems," *IEEE Trans. Very Large Scale Integr. (VLSI) Syst.*, vol. 26, no. 5, pp. 945–957, May 2018.

[8] X. Yi et al., "A 24/77 GHz dual-band receiver for automotive radar applications," *IEEE Access*, vol. 7, pp. 48053–48059, 2019.

[9] J. Davidse, "Characteristics of growth and limitations in electronics," *Technological Forecasting Social Change*, vol. 24, no. 2, pp. 125–135, Oct. 1983.

[10] X. S. Yao and L. Maleki, "Optoelectronic microwave oscillator," *J. Opt. Soc. Am. B*, vol. 13, no. 8, p. 1725, Aug. 1996.

[11] L. Maleki, "The optoelectronic oscillator," *Nature Photon.*, vol. 5, no. 12, pp. 728–730, Dec. 2011.

[12] K. Volyanskiy, Y. K. Chembo, L. Larger, and E. Rubiola, "Contribution of laser frequency and power fluctuations to the microwave phase noise of optoelectronic oscillators," *J. Lightw. Technol.*, vol. 28, no. 18, pp. 2730–2735, Sep. 15, 2010.

[13] D. Eliyahu, D. Seidel, and L. Maleki, "RF amplitude and phase-noise reduction of an optical link and an opto-electronic oscillator," *IEEE Trans. Microw. Theory Techn.*, vol. 56, no. 2, pp. 449–456, Feb. 2008.

[14] D. Eliyahu, K. Sariri, J. A. Taylor, and L. Maleki, "Optoelectronic oscillator with improved phase noise and frequency stability," *Proc. SPIE*, vol. 4998, pp. 139–147, Jul. 2003.

[15] X. S. Yao, L. Maleki, Y. Ji, G. Lutes, and M. Tu, "Dual-loop opto-electronic oscillator," in *Proc. IEEE Int. Freq. Control Symp.*, Pasadena, CA, USA, May 1998, pp. 545–549.

[16] H. Peng et al., "Tunable DC-60 GHz RF generation utilizing a dual-loop optoelectronic oscillator based on stimulated Brillouin scattering," *J. Lightw. Technol.*, vol. 33, no. 13, pp. 2707–2715, Jul. 1, 2015.

[17] J. Zhang and J. Yao, "Parity-time–symmetric optoelectronic oscillator," *Sci. Adv.*, vol. 4, no. 6, Jun. 2018, Art. no. eaar6782.

[18] Z. Ge, T. Hao, J. Capmany, W. Li, N. Zhu, and M. Li, "Broadband random optoelectronic oscillator," *Nature Commun.*, vol. 11, no. 1, Nov. 2020, Art. no. 5724.

[19] T. Hao et al., "Breaking the limitation of mode building time in an optoelectronic oscillator," *Nature Commun.*, vol. 9, no. 1, May 2018, Art. no. 1839.

[20] P. Devgan, "A review of optoelectronic oscillators for high speed signal processing applications," *Int. Scholarly Res. Notices*, vol. 2013, Apr. 2013, Art. no. 401969.

[21] X. Zou et al., "Optoelectronic oscillators (OEOs) to sensing, measurement, and detection," *IEEE J. Quantum Electron.*, vol. 52, no. 1, pp. 1–16, Jan. 2016.

[22] S. Liu, C. Du, L. Yang, M. Liu, Z. Tang, and S. Pan, "Coherent dual-frequency signal generation in an optoelectronic oscillator," *Opt. Lett.*, vol. 48, no. 11, pp. 2921–2924, Jun. 2023.

[23] Z. Fu et al., "Wide-range tunable coherent dual-frequency microwave signal generation with low spurious components in optoelectronic oscillator," *J. Lightw. Technol.*, vol. 42, no. 21, pp. 7443–7450, Nov. 1, 2024.

[24] E. C. Levy and M. Horowitz, "Single-cycle radio-frequency pulse generation by an optoelectronic oscillator," *Opt. Exp.*, vol. 19, no. 18, pp. 17599–17608, Aug. 2011.

[25] Z. Zeng et al., "Multi-format microwave signal generation based on an optoelectronic oscillator," *Opt. Exp.*, vol. 29, no. 19, p. 30834, Sep. 2021.

[26] J. Wo, J. Zhang, and Y. Wang, "Actively mode-locked optoelectronic oscillator for microwave pulse generation," *Opt. Laser Technol.*, vol. 146, Feb. 2022, Art. no. 107563.

[27] J. Zhang et al., "Tunable microwave pulse generation based on an actively mode-locked optoelectronic oscillator," *Photonics*, vol. 9, no. 10, p. 772, Oct. 2022.

[28] B. Yang, J. Yu, H. Chi, S. Yang, Y. Zhai, and J. Ou, "Polarization multiplexed active mode-locking optoelectronic oscillator for frequency tunable dual-band microwave pulse signals generation," *Opt. Exp.*, vol. 30, no. 15, pp. 27132–27139, Jul. 2022.

[29] Z. Wang, Y. Xie, Z. Wei, D. V. Plant, and L. R. Chen, "Versatile optoelectronic oscillator for single-frequency, dual-frequency, and mode-locking oscillation," *J. Lightw. Technol.*, vol. 43, no. 14, pp. 6554–6562, Jul. 15, 2025.

[30] A. Banerjee, L. A. D. de Britto, and G. M. Pacheco, "A theoretical and experimental study of injection-locking and injection-pulling for opto-electronic oscillators under radio frequency signal injection," *J. Lightw. Technol.*, vol. 38, no. 6, pp. 1210–1220, Mar. 15, 2020.

[31] H. Darabi and A. A. Abidi, "Noise in RF-CMOS mixers: A simple physical model," *IEEE J. Solid-State Circuits*, vol. 35, no. 1, pp. 15–25, Jan. 2000.

[32] C. D. Hull and R. G. Meyer, "A systematic approach to the analysis of noise in mixers," *IEEE Trans. Circuits Syst. I, Fundam. Theory Appl.*, vol. 40, no. 12, pp. 909–919, Dec. 1993.

[33] I. Rutkowski and K. Czuba, "Additive phase-noise in frequency conversion in LLRF systems," 2018, *arXiv:1806.09247*.

[34] T. Xie et al., "A flexibly frequency switchable active mode-locking optoelectronic oscillator with supermode noise suppression," *Opt. Laser Technol.*, vol. 163, Aug. 2023, Art. no. 109354.

[35] Z. Zeng et al., "Harmonically mode-locked optoelectronic oscillator with ultra-low supermode noise," *Opt. Laser Technol.*, vol. 151, Jul. 2022, Art. no. 108036.

[36] M. Kaveh and G. R. Cooper, "Average ambiguity function for a randomly staggered pulse sequence," *IEEE Trans. Aerosp. Electron. Syst.*, vols. AES–12, no. 3, pp. 410–413, May 1976.

[37] A. A. Alford, M. I. Biggerstaff, C. L. Ziegler, D. P. Jorgensen, and G. D. Carrie, "A method for correcting staggered pulse repetition time (PRT) and dual pulse repetition frequency (PRF) processor errors in research radar datasets," *J. Atmos. Ocean. Technol.*, vol. 39, no. 11, pp. 1763–1780, Nov. 2022.

[38] Y. Zhang et al., "Actively mode-locked modulator-free optoelectronic oscillator for multi-functional microwave pulse generation," *J. Lightw. Technol.*, vol. 42, no. 19, pp. 6760–6766, Oct. 1, 2024.